INORGANIC CHEMISTRY
FRONTIERS

CHINESE CHEMICAL SOCIETY

ROYAL SOCIETY OF CHEMISTRY

RESEARCH ARTICLE

View Article Online
View Journal | View Issue

Check for updates

Cite this: *Inorg. Chem. Front.*, 2024, **11**, 3777

Design and synthesis of a deep-cavity aluminium-organic macrocycle to trap dyes and generate enhanced non-linear optical performance†

Zhuang-Hua Liu,[a] Si-Hao Shen,[a] Cheng-Yang Zhang,[a] Jingyang Niu,[b] Qiao-Hong Li,*[a] Jian Zhang[a] and Wei-Hui Fang*[a]

Received 17th April 2024,
Accepted 13th May 2024

DOI: 10.1039/d4qi00976b

rsc.li/frontiers-inorganic

The development of a "two birds with one stone" strategy for capturing pollutant molecules and incorporating new functions provides a promising solution for sustainability. In this work, we designed an unprecedented deep-cavity aluminum–organic macrocycle to trap dye molecules and enhance non-linear optical performance. Using long building blocks and inorganic aluminum ions at the midriff, we successfully isolated a deep-cavity (1.8 nm) macrocycle, with a deeper cavity than classic pure organic macrocycles, such as crown ether and calixarenes. We report the accurate locking of the HAO7 dye molecule in the deep-cavity macrocycle and reveal its trapping mechanism at the molecular level for the first time. The combined host–guest compound **AlOC-136-HAO7** displays altered physical properties, such as a decreased optical band gap and increased proton conductivity but also exhibits enhanced third-order non-linear optical (NLO) properties. Combined with theoretical calculations, we confirmed that the enhancement was attributed to abundant host–guest interactions and the guest-to-guest charge transfer. Our findings provide a strategy for isolating deep-cavity macrocycles and further demonstrate their enormous potential for capturing contaminants and forming valuable materials.

Introduction

In recent years, water contamination with dyes from industries has become a global concern.[1] This is not only due to vast amounts discharged (global emissions are nearly 80 000 tons per year) but also because of the toxicity[2] and resistance to biodegradation (*i.e.*, the half-life of hydrolyzed reactive blue 19 is about 46 years) of dyes.[3] Particular attention should be given to azo dyes[4,5] because they are the most commonly used chromophore and account for up to 70% of all produced textiles. Compared with chemical methods,[6–9] physical adsorption is generally considered a more efficient, low-cost, and environmentally friendly method for removing dyes from wastewater.[10–12] Ideally, adsorbents should be designed to utilize these trapped or adsorbed dyes to realize "Waste to Wealth". According to some recent research, such an idea is not a castle in the sky. It has been reported that confining conjugated photonic active dye molecules in metal–organic frameworks with regular internal cavities could help amplify their function and minimize aggregation-caused quenching effects.[13,14]

The first step in turning "Waste to Wealth" is to design periodic shape-matched cavities that can simultaneously be beneficial for investigating the adsorption mechanism. In terms of crystalline materials, macrocycles, famous for their central cavities for guest inclusion, are promising candidates. Recent research on macrocycle-dye complexes has been carried out in aqueous solution,[15] while their unambiguous host–guest interaction in the solid state is relatively challenging because the specific structures of shallow cavity macrocycles interact very weakly with the dyes. Therefore, one solution is constructing a cavity that is deep enough to bury the dyes. The next step that we should consider is how to transform host–guest compounds into functional materials. Despite extensive study and advances in large-cavity macrocycles,[16–19] those with deep and stable cavities are far from abundant.

Based on above presented considerations and our recent extensive research regarding aluminium molecular rings,[20–24] we are particularly interested in designing deep-cavity macrocycles to realize "Waste to Wealth". Although we have developed efficient synthetic strategies for the isolation of aluminum molecular rings, most of these are shallow molecular rings lacking a sufficient buried surface area to encapsulate large-sized guest

---

[a] *State Key Laboratory of Structural Chemistry, Fujian Institute of Research on the Structure of Matter, Chinese Academy of Sciences, 350002 Fuzhou, P.R. China. E-mail: lqh2382@fjirsm.ac.cn, fwh@fjirsm.ac.cn*

[b] *Henan Key Laboratory of Polyoxometalate, College of Chemistry and Molecular Science, Henan University, 475004 Kaifeng, P.R. China*

† Electronic supplementary information (ESI) available: Experimental section, detail structure charts, stability analysis, characterization, tables and supplement videos. CCDC 2304752 (**AlOC-136**) and 2304753 (**AlOC-136-HAO7**). For ESI and crystallographic data in CIF or other electronic format see DOI: **https://doi.org/10.1039/d4qi00976b**

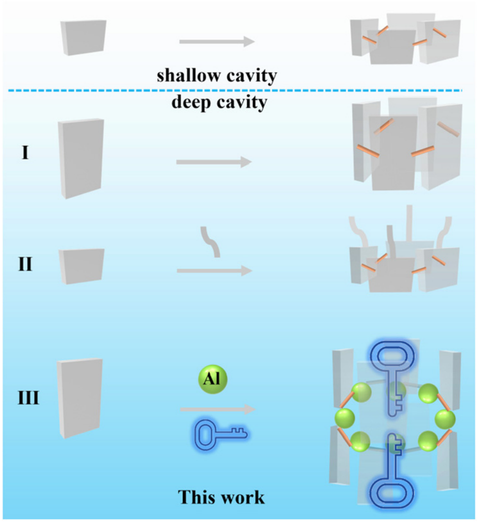

Scheme 1 Diagram showing the designable assembly of macrocycles. There are three strategies to obtain deep-cavity macrocycles: (I) self-assembly cyclization achieved using long building blocks; (II) postmodification (that is, extending the cavity depth of an existing macrocycle); and (III) self-assembly cyclization as achieved in this work using long building blocks and inorganic aluminum ions, which can trap linear dyes.

molecules. Inspired by the two methods that are currently commonly used, self-assembly cyclization by long building blocks[25,26] and postmodification[27–29] (extending the cavity depth of an existing macrocycle), we herein aim to create a deep-cavity inorganic–organic macrocycle by employing long building blocks and inorganic aluminum ions at the midriff (Scheme 1). Considering the linear and aromatic characteristics of dye molecules, we chose the long linear ligand indole-2-carboxylic acid (HL 7.3 Å) to simultaneously act as pillars for constructing deep cavities and bring potential photo-related applications. The choice of azo dyes as the target is due to their large proportion in production applications and their enormous potential as non-linear optical (NLO) materials due to red-shifted absorption maxima, large dipole moments, and good thermal stability.[30,31]

Thus, we designed and synthesized a macrocycle with a deep cavity depth of approximately 2 nm to lock Acid Orange 7 (NaAO7) molecules in a 1 : 2 ratio and simultaneously enhance optical performance. It is worth noting that the host–guest interactions are unambiguously revealed by single-crystal X-ray diffraction. Such a "lock and key" host–guest complex possesses a low band gap and notably better third-order nonlinear optical (NLO) effect than those of separate pristine component materials and physically doped materials.

Results and discussion

Assembly of deep-cavity aluminum–organic macrocycles and structural characterization

First, we reviewed the aluminium–organic molecular rings synthesized in recent years. We found a clear trend, whereby the macrocycles with alcohol ligands are shallow and those containing only one type of aromatic carboxylic acid ligand have a large dihedral angle (between the ligand and aluminum inorganic ring plane) (Fig. 1a) and deeper cavity. Our literature investigation of all metal–organic ring molecules showed that although some also have large dihedral angles,[32–36] most of them are fatty carboxylic acid ligands[37–39] and have not formed regular deep cavities.[40–42] First, under the regulation of alcohol solvents, despite employing long ligands, we consistently obtained similar shallow rings, concordant with the pattern mentioned above. Therefore, when designing and synthesizing deep-cavity macrocycles, selecting the right solvent and using long aromatic ligands are crucial. This review and discussion provide a foundation for this work's design and synthesis of metallocycles with deep cavities.

Colorless decahedral crystals of $[Al_8(OH)_8L_{16}]$ (**AlOC-136**) were readily obtained in considerable yield by reacting aluminum isopropoxide and indole-2-carboxylic acid (HL) in a stoichiometric ratio (1 : 2) in the presence of acetonitrile. Acetonitrile effectively prevents the generation of products that are similar to previous shallow bowl-shaped metallocycles.[20,23] Single-crystal X-ray diffraction (SCXRD) analysis revealed that **AlOC-136** is an eight-membered macro-metallocycle with eight bridging –OH pointing into the center (Fig. 1b and c) and crystallizes in the *P*4*nc* space group (Table S1†). The asymmetric unit of **AlOC-136** includes two Al(III) centers, four L ligands, and two μ_2-OH groups (Fig. S1a†).

Its most prominent structural feature is the presence of a cavity with a depth of around 1.8 nm, which is significantly larger than that observed in many classic pure organic macrocycles (Fig. 1b and d, and Table S2†).[17,25,43–48] **AlOC-136** possesses the greatest depth among all the cyclic compounds in the system (Fig. S2 and S3†). The octahedral coordination geometry of aluminum is completed by a deprotonated L ligand, resulting in 16 L ligands surrounding each metallocycle (Fig. 1c and Fig. S1†). Intuitively, these ligands can be divided into axial position (labeled as α, β) and equatorial position (labeled as γ, η) (Fig. 1b). From the top view, the outer diameter of the ring is 2.5 nm, defined as the distance between two equatorial positions (γ or η) ligands, while the inner diameter is 0.5 nm, defined as the distance between two opposite –OH (Fig. 1c). The inner diameter of the aluminum molecular macrocycles is similar to that of α-cyclodextrin,[49] larger than that of crown[50] and smaller than that of non-porous pillar[*n*]arene (Table S2†).[17,51] From the side view, four ligands in the α position form a calixarene-like cavity (defined as the α-cavity), while four ligands in the β position form the β-cavity (Fig. 1b). Thus, an hourglass-shaped macrocycle is formed with two large hydrophobic ends and a small middle hydrophilic cavity. Its dimensions are 0.8 nm and 1.1 nm for upper-rim lengths, 0.5 nm and 0.8 nm for lower-rim sizes (that is, distances between the centers of the benzene rings of indole unit) (Fig. S4†), which stems from the difference in the dihedral angle (75° *vs.* 85°) (Fig. 1a and Fig. S5†). **AlOC-136** not only has deep intramolecular cavities (404 Å^3, the sum of two α-cavities) (Fig. 1b and Fig. S6†) but also intermolecular pores (27.1%

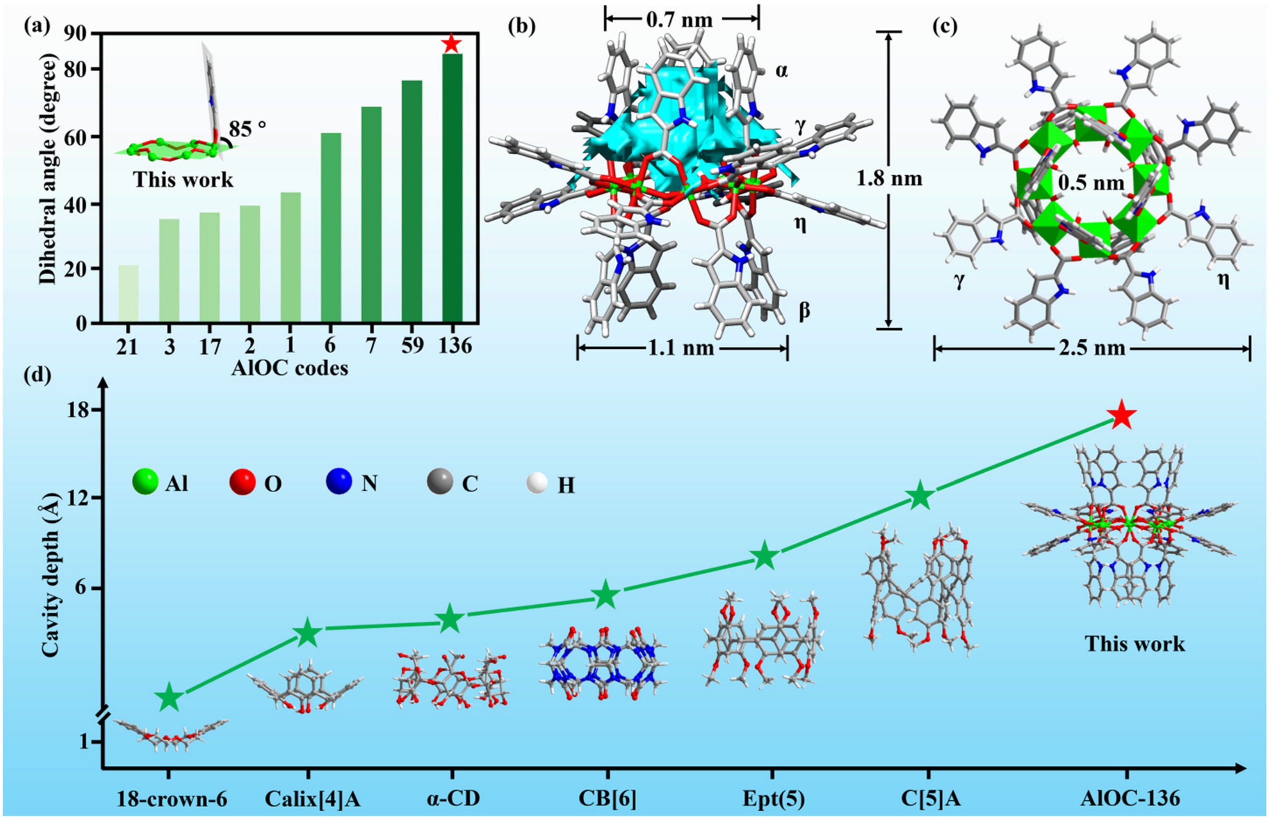

Fig. 1 Molecular structure of **AlOC-136**. (a) A summary of the dihedral angles of the aluminum molecular rings. The dihedral angles between the ligand and aluminum inorganic ring plane of representative rings were calculated and are displayed in the form of a bar chart in order from the smallest to largest. (b) Side view of **AlOC-136** showing two hydrophobic cavities. The ligands in the α and β positions form two calixarene-like cavities with different sizes because of the different dihedral angles. The surface and volume of the α-cavity were calculated *via* the 3 V Volume Assessor program. The calculated surface area is 423 Å^2, and the calculated volume is 202 Å^3. (c) The top octahedral view of the **AlOC-136** with an outer diameter of 2.5 nm and inner hydrophilic cavity with a diameter of 0.5 nm. (d) A summary of cavity depth from classic pure organic macrocycles to inorganic–organic **AlOC-136**.

according to PLATON calculations) to provide space for guest inclusion (Fig. S6c†). Gas adsorption further demonstrated that **AlOC-136** has a permanent microporous structure. Nitrogen adsorption–desorption isotherms collected at 77 K on activated **AlOC-136** exhibited type I behavior (Brunauer–Emmett–Teller (BET) surface area is 371 m^2 g^{-1}) (Fig. S6d†).

$$8\mathrm{Al(O^iPr)_3} + 16\mathrm{HL} + 8\mathrm{H_2O} \rightarrow [\mathrm{Al_8(L)_{16}(OH)_8}] + 24\mathrm{HO^iPr}$$

Adsorption performance for dye molecules by deep-cavity aluminium–organic macrocycle

To verify the structural stability of **AlOC-136**, we immersed the crystal sample of **AlOC-136** in an aqueous solution with pH values ranging from 2–7 and common organic solvents. The powder X-ray diffraction (PXRD) results confirm its air and water structural stability (Fig. S17 and S18†). The single-crystal X-ray diffraction images prove that **AlOC-136** maintains good diffraction points after soaking in aqueous acidic solution and organic solvents such as toluene, ethanol, cyclohexane, DMSO, DCM, and petroleum ether for 48 h (Fig. S20 and S21†). This water stability is attributed to the abundance of hydrophobic groups on its structural surface, as demonstrated by its large contact angle observed in the wettability investigation (Fig. S22†). Considering the inherent deep-cavity tubular structure of the compound, water stability, and facile synthesis (Fig. 3a), we performed adsorption experiments with Acid Orange 7 (NaAO7), Alizarin Yellow (AY), and Acid Red 27 (AR27) azo dye molecules at 60 °C in water (Fig. S23†). The hybrid deep-cavity macrocycle exhibited superior adsorption of NaAO7 molecules (Fig. S24†), which may stem from the linear-shaped geometry and different hydrophilic and hydrophobic features of the two ends. This result encouraged us to study its capture mechanism. However, attempts to determine its microscopic capture principle through immersion experiments were unsuccessful because crystallization remained while no suitable peak could be defined as NaAO7 molecules after immersion (defined as **AlOC-136′**, Table S1†).

To clarify the NaAO7 capture mechanism, we tried the cocrystallization method. Fortunately, the red flaky single crystals of **AlOC-136-HAO7** were successfully isolated. The one-pot approach closely relates to the proposed mechanism whereby anionic dye (AO7) tends to be removed using a highly acidic solution.[52] We speculate that excess HL acid ligands during synthesis create an acidic reaction environment (pH ≈ 4) to form protonated HAO7, which drives the host–guest combination process. Such speculation is confirmed by isolating the same host–guest product using other acidic substances, such as aluminum chloride and methylacrylic acid. A more intuitive analysis comes from the electrostatic potential map (ESP) calculation (Fig. 2c).[53] We discovered that the hydrophilic center of the cavity of **AlOC-136** is highly electropositive (0.06), and should thus be inclined to interact with the protonated HAO7 species. For the first time, we made a clear elucidation at the molecular level, as the mechanism of anionic AO7 capture has been speculative for a long time.[54]

Single-crystal analysis showed that **AlOC-136-HAO7** crystallized in the *C*2/*c* space group (ESI video S1†). Its asymmetric unit included five Al(III) centers, eight L ligands, a protonated AO7 guest molecule (HAO7), and four –OH, as well as two acetonitrile molecules and two water molecules as guests (Fig. S7†). Notably, **AlOC-136-HAO7** has significant host–guest interactions and apparent adaptive behavior. On the one hand, different kinds of guest molecules are comfortably located in various positions owing to their different size and structural characteristics. The small molecule guests of acetonitrile and water interact adhesively in the hydrophobic voids between macrocyclic molecules (Fig. S8†) through hydrogen bonding (Fig. S9 and Table S3†). The linear-shaped HAO7 molecules are partially wrapped in deep-cavity rings with the hydrophilic sulfonic group facing inward and hydrophobic naphthalene facing outward, consistent with the hydrophilic characteristics of the central cavity. As can be seen from Fig. 2a, each large ring captures two HAO7 molecules (the naphthol ring on HAO7 has a statistical phenomenon) that exhibit a torsion angle of 90° (Fig. S10†), which is caused by a 45° misalignment of aromatic hydrophobic walls in the upper and lower parts of the cavity (Fig. S11†). This combination of host and guest is attributed to shape matching and four different host–guest forces (summarized in Table S4†), namely: (I) strong hydrogen bonding (O–H···O, 2.6–2.7 Å) between the sulfonic group and hydrophilic –OH site in the center of the ring; (II) sandwich-configuration π–π (3.9–4.0 Å) and T-shape configuration π–π interactions (4.7–4.9 Å) (Fig. S12†) between the benzoate ring of HAO7 and hydrophilic aromatic walls of the ring; (III) hydrogen bond interactions between the azo moiety and ing body (C–H···N, 3.3–3.8 Å); and (IV) the naphthol ring on HAO7 extends out of the central cavity involving abundant C–H···π interactions (3.3–3.8 Å) with the ligand aromatic ring in the perpendicular and equatorial directions of the adjacent aluminum ring (Fig. 2b and Fig. S13†). Furthermore, the ring host adapts to the most comfortable state with the entry of the HAO7 molecule. The shape of the annular cavity changed significantly from different sizes at both the ends to the same length (Fig. S14†), which is also related to the host–guest adaptation described above. To determine the quantitative distribution of these weak interaction forces, we used Hirshfeld surface analysis[55] (Fig. S25†) to calculate the bond energy relationship within or between molecules (see the 2D fingerprint plot in Fig. S26†). Compared with the pristine -AB- alternating supramolecular stacking in **AlOC-136**, the compound **AlOC-136-HAO7** exhibits A-type stacking after the trapping of the HAO7 guest (retaining a porosity of 21%) (Fig. S15 and S16†).

$$8\mathrm{Al(O^iPr)_3} + 16\mathrm{HL} + 8\mathrm{H_2O} + 2\mathrm{NaAO7} \rightarrow [\mathrm{Al_8(L)_{16}(OH)_8}\cdot 2(\mathrm{HAO7})] + 22\mathrm{HO^iPr} + 2\mathrm{NaO^iPr}$$

In addition to the single-crystal analysis method described above to provide visual evidence for capturing

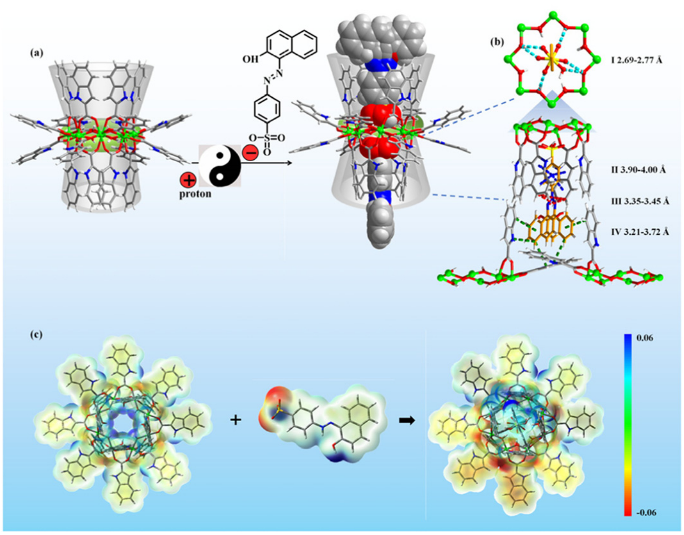

Fig. 2 Molecular structure of **AlOC-136-HAO7**. (a) *In situ* self-assembly strategy of **AlOC-136-HAO7**. (b) Host–guest interactions. The central HAO7 guest molecule is emphasized in space-filling mode for clarity. (c) Electrostatic potential (ESP) maps of **AlOC-136** (left), NaAO7 (middle), and **AlOC-136-HAO7** (right) molecules. Areas of low potential, red, are characterized by an abundance of electrons. Areas of high potential, blue, are characterized by a relative absence of electrons.

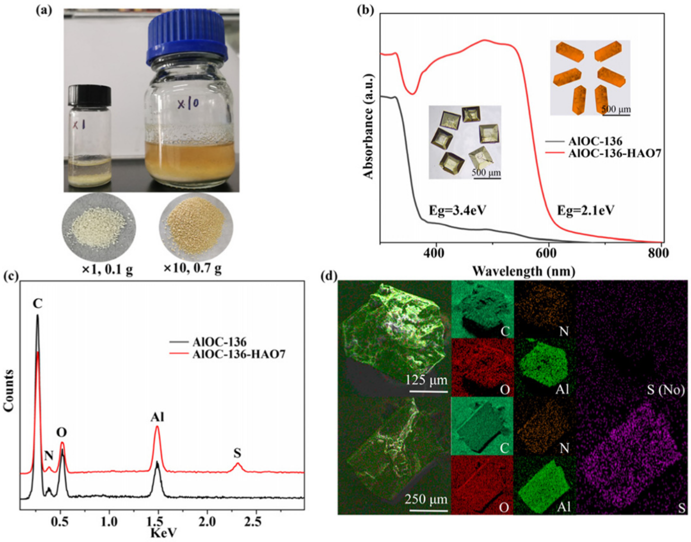

Fig. 3 Scale-up synthesis and solid phase characterization. (a) Scale-up synthesis for **AlOC-136**. Add ten times the ratio of the pristine material in the blue cap bottle and heat at 100 °C for 48 h to get about 700 mg of **AlOC-136**. (b) Solid-state absorption spectra. Inset are crystal photos of **AlOC-136** (left) and **AlOC-136-HAO7** (right). (c) EDS spectra prove the presence of S in **AlOC-136-HAO7**, a characteristic element of HAO7. (d) After cutting, the EDS-mapping spectra from the central cross-section of **AlOC-136** (top) and **AlOC-136-HAO7** (bottom). The S element is evenly distributed in **AlOC-136-HAO7**.

HAO7 molecules, we obtained additional evidence from the bulk sample. The first manifestation is its significant color change from colorless to red (Fig. 3b). In addition, two other direct pieces of evidence of the presence of HAO7 come from energy dispersive spectroscopy (EDS) and Fourier transform infrared (FT-IR) spectroscopy. EDS proved the presence of S, a characteristic element of HAO7 (Fig. 3c and d). The absorption peak at 1031 cm^{-1} is attributed to the symmetric O═S═O stretching vibration of $-SO_3H$ groups[56] in **AlOC-136-HAO7** (Fig. S27 and S28†). The physical properties of the macrocycle changed significantly after the capture of the guest molecule, mainly reflected in the decreased optical band gap and wettability, improved thermal stability, and increased proton conductivity. The solid-state UV-vis diffuse reflection data indicates that the band gap energy reduces from 3.4 eV (**AlOC-136**) to 2.1 eV (**AlOC-136-HAO7**), which is consistent with the color change (Fig. 3b). The thermogravimetric (TGA) curve shows that **AlOC-136-HAO7** exhibits better thermal stability than that of **AlOC-136** (Fig. S29 and S30†). Since hydrophilic $-SO_3H$ groups are confined within the ring, the contact angle of **AlOC-136-HAO7** is lower than that of **AlOC-136** (Fig. S22†). Considering that the $-SO_3H$ group has been recognized as a superior proton donor and an enabler for high proton conductivity,[56,57] we investigated the proton conductivity (Fig. S31†). The results showed that the bulk conductivity of **AlOC-136-HAO7** is six orders of magnitude higher than that of vacant **AlOC-136**, increasing from 6.7×10^{-9} S cm^{-1} to 7.78×10^{-3} S cm^{-1} at 98 °C and 98% RH. Activation energies (E_a) of the materials were derived from Arrhenius plots to be 0.23 eV for **AlOC-136-HAO7** (Fig. S32†), indicating that the proton transfer follows the conventional Grotthuss mechanism.[58]

Improved third-order non-linear optical properties

The introduction of HAO7 decreases the optical band gap and wettability, increases the thermal stability and proton conductivity, and brings new functions. Taking into account weak interactions, especially π⋯π interactions that might contribute to optical properties, we further investigated the third-order NLO properties. As control experiments, we performed same tests on the pristine constitute component, including the blank **AlOC-136** macrocycle and NaAO7 powder, as well as physically doped materials (that is, a mixture of ground powder of **AlOC-136** and NaAO7 with the same chemical molar ratio of 1 : 2).

The third-order NLO properties and optical limiting (OL) activities were investigated through a facile *Z*-scan technique, which is widely applied for analyzing the NLO response due to its simplicity, suitable operation, and high sensitivity (Fig. 4a). By dispersing uniformly in *N*,*N*-dimethylformamide (DMF) solution (Fig. 4b), **AlOC-136** showed an unobvious NLO response even though there are conjugated ligands on the molecular ring, which is possibly due to the lack of intramolecular interactions and relatively weak intermolecular π conjugation interactions. As shown in Fig. 4c, the OA *Z*-scan curves of **AlOC-136-HAO7**, NaAO7 powder, and physically doped material exhibited an apparent saturation absorption (SA) response, which results from the surface defect effect, the quantum confinement effect, and complex interactions between molecules.[59,60] OL curves confirmed that the normal-

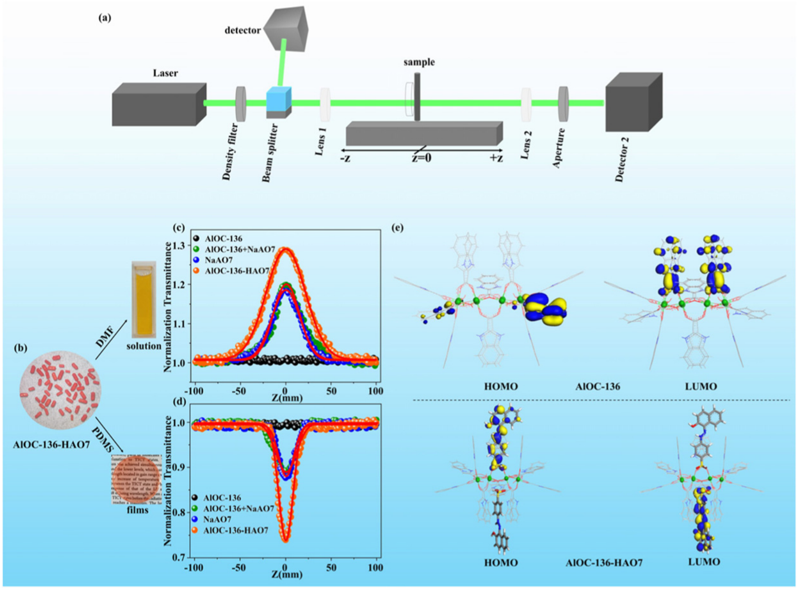

Fig. 4 NLO investigation. (a) Schematic representation of the *Z*-scan setup. (b) Sample preparation methods in different media. The figure shows **AlOC-136-HAO7** as an example. (c) OA *Z*-scan curves of samples dispersed in DMF solution with nanosecond laser duration excitation (input energy: 100 μJ). (d) OA *Z*-scan curves of samples dispersed in PDMS films with nanosecond laser duration excitation (input energy: 100 μJ). (e) The frontier molecular orbital theoretical view of the HOMO and LUMO states of **AlOC-136** and **AlOC-136-HAO7**.

ized transmittance of samples depends on the input laser pulse energy according to eqn (1):

$$F_{\mathrm{in}}(z) = \frac{4\sqrt{\ln 2 - E_{\mathrm{in}}}}{\pi^{\frac{3}{2}}\omega(z)^2}, \tag{1}$$

where $F_{\mathrm{in}}(z)$ is the position-dependent light fluence at any position z, E_{in} is the input laser pulse energy (Fig. S33a†), and the beam radius $w(z)$ is given by:

$$\omega(z) = \omega(0)\sqrt{1+\left(\frac{z}{z_0}\right)^2} \tag{2}$$

Among them, **AlOC-136-HAO7** gave the most prominent SA response and had the largest normalized transmittance of ≈1.28 at the laser focus, where the input fluence is at its maximum. Moreover, the output fluence of **AlOC-136-HAO7** linearly increased at low-incident fluence. However, it deviates from the linearity at high-incident fluence, which indicates the typical OL effect (Fig. S33b†). Furthermore, to quantitatively evaluate the NLO effects of the samples, NLO absorption coefficients were obtained by fitting open aperture *Z*-scan curves using eqn (3):[61]

$$T(z, s=1) = \frac{1}{\sqrt{\pi}q_0(z,0)}\int_{-\infty}^{\infty}\ln[1+q_0(z,0)e^{-r^2}]\mathrm{d}r \tag{3}$$

here, $q_0(z,0) = \beta I_0 L_{\mathrm{eff}}$, where I_0 is the on-axis peak intensity at the focus (z = 0), $L_{\mathrm{eff}} = [1 - \exp(-\alpha l)/\alpha]$ is the effective thickness of the sample, l is the sample thickness and α is the linear absorption coefficient $\left(\alpha = \ln\left(\frac{1}{T}\right)/l\right)$. The non-linear absorption coefficient β value for **AlOC-136-HAO7** is −15.98 cm per GW, as listed in Table S5.† It is superior to the majority of azo dyes,[62] although it is not comparable with transition metal-based materials.[63] Besides, the imaginary part of the third-order non-linear optical susceptibility $\mathrm{Im}\chi^{(3)}$ was calculated according to eqn (4):

$$\mathrm{Im}\chi^{(3)} = \left[\frac{10^{-7}c\lambda n^2}{96\pi^2}\right]\cdot\beta, \tag{4}$$

where c is velocity of light, λ is the wavelength of the incident light and n is the refractive index, and FOM was calculated by $\left|\frac{\mathrm{Im}\chi^{(3)}}{\alpha}\right|$ (Table S5†). The expected results were consistent with the analysis of the host–guest interactions in the previous structural description. Such performance originates from HAO7 molecules because blank **AlOC-136** only exhibits a weak signal. However, we can see that the physically doped material displays close the NLO effects to those of the NaAO7 powder.

To achieve devices for practical OL application, we prepared transparent and flexible films by evenly dispersing the samples into a polydimethylsiloxane (PDMS) matrix (Fig. 4b). Compared with the solution method, it is worth noting that **AlOC-136-HAO7** exhibited an opposite reverse saturable absorption (RSA) response (Fig. 4d and Fig. S34, Table S6†) but with the same trend. This phenomenon was also observed in Zhan's system research of nanostructured noble metals[64] and is related to the hindered electronic relaxation process in solid-state environments.[65] Considering that **AlOC-136-HAO7** reveals an SA response (applied in fast optical switching and passive mode-locking technique) and RSA response (applied in protecting human eyes and sensitive optical devices) in different matrices, we could prepare devices according to requirements.

Considering why such chemical doping with precise host–guest structure behaves better than physical doping, we suspect it is related to periodic structures with confined effects. To further clarify this, we performed density-functional theory (DFT) calculations. In the **AlOC-136** macrocycle, the highest occupied molecular orbital (HOMO) is composed of equatorial position ligands, while the lowest unoccupied frontier (LUMO) is composed of the axial position ligand (Fig. 4e). However, in **AlOC-136-HAO7**, the guest-to-guest charge transfer is between the two linear HAO7 molecules (Fig. 4e). Therefore, combining structural analysis and theoretical calculations, the enhancement of NLO behaviour could be attributed to the periodic abundant host–guest interactions and guest-to-guest charge transfer.[66]

Conclusions

In summary, we have demonstrated the designed synthesis of a deep-cavity aluminum–organic macrocycle (**AlOC-136**) with a hydrophobic inner wall and hydrophilic center. The crucial factors for the generation of deep-cavity aluminum–organic macrocycles lie in introducing more extended ligands and selecting aprotic solvents. Combined with the feature of a deep cavity, we explored an *in situ* self-assembly strategy to capture linear dye Acid Orange 7 (**AlOC-136-HAO7**) and revealed the HAO7 capture mechanism at the molecular level for the first time. NLO experiment results illustrated that **AlOC-136-HAO7** exhibited significantly enhanced NLO behavior compared with pristine constituent components and physically doped components. Theoretical calculations demonstrated that the enhancement of NLO behavior could be attributed to the guest-to-guest charge transfer. In addition, **AlOC-136-HAO7** realized SA and RSA response conversion in different matrices, which could play a corresponding role in diverse environments. This work brings a bright future for the promising inorganic–organic hybrid deep-cavity macrocycle system, reveals their particular application in guest capture, and incorporates valuable functions.

Data availability

The datasets supporting this article have been uploaded as part of the ESI.† X-ray crystallographic data for the structures reported in the article have been deposited at the Cambridge Crystallographic Data Centre, under deposition numbers CCDC 2304752 (**AlOC-136**) and 2304753 (**AlOC-136-HAO7**).† The dataset is also provided as ESI† with this paper. All other data supporting the findings of this study are available within the paper and its ESI† and from the corresponding author.

Author contributions

All authors contributed extensively to the work presented in this paper. W.-H. F., J. N. and J. Z. conceived and designed this project. Z.-H. L. carried out the synthesis, characterization and non-linear optical study. S.-H. S. assisted with proton conductivity measurements. Q.-H. Li carried out the theoretical calculations. C.-Y. Z. gave support on the writing. W.-H. F. and Z.-H. L. wrote the manuscript. All the authors discussed the results and commented on the manuscript.

Conflicts of interest

There are no conflicts to declare.

Acknowledgements

This work is supported by the National Natural Science Foundation of China (22371278, U23A2095, and 92061104), Natural Science Foundation of Fujian Province (2021J06035) and Youth Innovation Promotion Association Chinese Academy of Sciences (Y2021081).

References

1 M. A. Hassaan, A. El Nemr and A. Hassaan, Health and Environmental Impacts of Dyes: Mini Review, *Am. J. Environ. Sci. Eng.*, 2017, **1**, 64–67.

2 J. Liang, X.-a. Ning, J. Sun, J. Song, J. Lu, H. Cai and Y. Hong, Toxicity evaluation of textile dyeing effluent and its possible relationship with chemical oxygen demand, *Ecotoxicol. Environ. Saf.*, 2018, **166**, 56–62.

3 O. J. Hao, H. Kim and P.-C. Chiang, Decolorization of Wastewater, *Crit. Rev. Environ. Sci. Technol.*, 2000, **30**, 449–505.

4 A. M. M. Vargas, A. L. Cazetta, A. C. Martins, J. C. G. Moraes, E. E. Garcia, G. F. Gauze, W. F. Costa and V. C. Almeida, Kinetic and equilibrium studies: Adsorption of food dyes Acid Yellow 6, Acid Yellow 23, and Acid Red 18 on activated carbon from flamboyant pods, *Chem. Eng. J.*, 2012, **181–182**, 243–250.

5 A. M. M. Vargas, A. C. Martins and V. C. Almeida, Ternary adsorption of acid dyes onto activated carbon from flamboyant pods (Delonix regia): Analysis by derivative spectrophotometry and response surface methodology, *Chem. Eng. J.*, 2012, **195–196**, 173–179.

6 S.-F. Kang, C.-H. Liao and S.-T. Po, Decolorization of textile wastewater by photo-fenton oxidation technology, *Chemosphere*, 2000, **41**, 1287–1294.

7 E. J. Ruiz, C. Arias, E. Brillas, A. Hernández-Ramírez and J. M. Peralta-Hernández, Mineralization of Acid Yellow 36azo dye by electro-Fenton and solar photoelectro-Fenton processes with a boron-doped diamond anode, *Chemosphere*, 2011, **82**, 495–501.

8 Z. Xia, L. Wang, Q. Zhang, F. Li and L. Xu, Fast degradation of phenol over porphyrin-polyoxometalate composite photocatalysts under visible light, *Polyoxometalates*, 2022, **1**, 9140001.

9 Z. Ni, N. Liu, C. Zhao and L. Mi, Hexanuclear nickel-added silicotungstates as high-efficiency electrocatalysts for nitrate reduction to ammonia, *Polyoxometalates*, 2024, **3**, 9140044.

10 M. Sultan, Polyurethane for removal of organic dyes from textile wastewater, *Environ. Chem. Lett.*, 2017, **15**, 347–366.

11 S. Rojas and P. Horcajada, Metal–Organic Frameworks for the Removal of Emerging Organic Contaminants in Water, *Chem. Rev.*, 2020, **120**, 8378–8415.

12 A. Kausar, S. T. Zohra, S. Ijaz, M. Iqbal, J. Iqbal, I. Bibi, S. Nouren, N. El Messaoudi and A. Nazir, Cellulose-based materials and their adsorptive removal efficiency for dyes: A review, *Int. J. Biol. Macromol.*, 2023, **224**, 1337–1355.

13 H. He, E. Ma, Y. Cui, J. Yu, Y. Yang, T. Song, C.-D. Wu, X. Chen, B. Chen and G. Qian, Polarized three-photon-pumped laser in a single MOF microcrystal, *Nat. Commun.*, 2016, **7**, 11087.

14 H. Li, L. Zhang, H. He, Y. Yang, Y. Cui and G. Qian, Tunable nonlinear optical responses based on host–guest MOF hybrid materia, *Sci. China Mater.*, 2021, **64**, 698–705.

15 R. N. Dsouza, U. Pischel and W. M. Nau, Fluorescent Dyes and Their Supramolecular Host/Guest Complexes with Macrocycles in Aqueous Solution, *Chem. Rev.*, 2011, **111**, 7941–7980.

16 S. M. Biros and J. Rebek, Structure and binding properties of water-soluble cavitands and capsules, *Chem. Soc. Rev.*, 2007, **36**, 93–104.

17 K. Jie, Y. Zhou, Y. Yao and F. Huang, Macrocyclic amphiphiles, *Chem. Soc. Rev.*, 2015, **44**, 3568–3587.

18 Z. Liu, S. K. M. Nalluri and J. F. Stoddart, Surveying macrocyclic chemistry: from flexible crown ethers to rigid cyclophanes, *Chem. Soc. Rev.*, 2017, **46**, 2459–2478.

19 G. Zhang, W. Lin, F. Huang, J. Sessler and N. M. Khashab, Industrial Separation Challenges: How Does Supramolecular Chemistry Help?, *J. Am. Chem. Soc.*, 2023, **145**, 19143–19163.

20 L. Geng, C.-H. Liu, S.-T. Wang, W.-H. Fang and J. Zhang, Designable Aluminum Molecular Rings: Ring Expansion and Ligand Functionalization, *Angew. Chem., Int. Ed.*, 2020, **59**, 16735–16740.

21 S. Yao, W.-H. Fang, Y. Sun, S.-T. Wang and J. Zhang, Mesoporous Assembly of Aluminum Molecular Rings for Iodine Capture, *J. Am. Chem. Soc.*, 2021, **143**, 2325–2330.

22 C.-H. Liu, W.-H. Fang, Y. Sun, S. Yao, S.-T. Wang, D. Lu and J. Zhang, Designable Assembly of Aluminum Molecular Rings for Sequential Confinement of Iodine Molecules, *Angew. Chem., Int. Ed.*, 2021, **60**, 21426–21433.

23 Y. Li, C. Zheng, S.-T. Wang, Y.-J. Liu, W.-H. Fang and J. Zhang, Record Aluminum Molecular Rings for Optical Limiting and Nonlinear Optics, *Angew. Chem., Int. Ed.*, 2022, **61**, e202116563.

24 D. Luo, H. Xiao, M.-Y. Zhang, S.-D. Li, L. He, H. Lv, C.-S. Li, Q.-P. Lin, W.-H. Fang and J. Zhang, Accurate binding of porous aluminum molecular ring catalysts with the substrate, *Chem. Sci.*, 2023, **14**, 5396–5404.

25 H. Han, R. Fu, R. Wang, C. Tang, M.-M. He, J.-Y. Deng, D.-S. Guo, J. F. Stoddart and K. Cai, Corralarenes: A Family of Conjugated Tubular Hosts, *J. Am. Chem. Soc.*, 2022, **144**, 20351–20362.

26 X. Wan, S. Li, Y. Tian, J. Xu, L.-C. Shen, H. Zuilhof, M. Zhang and A. C.-H. Sue, Twisted pentagonal prisms: Ag_nL_2 metal-organic pillars, *Chem*, 2022, **8**, 2136–2147.

27 R. K. Juneja, K. D. Robinson, C. P. Johnson and J. L. Atwood, Synthesis and characterization of rigid, deep-cavity calix[4]arenes, *J. Am. Chem. Soc.*, 1993, **115**, 3818–3819.

28 S. M. Biros and J. J. Rebek, Structure and binding properties of water-soluble cavitands and capsules, *Chem. Soc. Rev.*, 2007, **36**, 93–104.

29 G. Peñuelas-Haro and P. Ballester, Efficient hydrogen bonding recognition in water using aryl-extended calix[4]pyrrole receptors, *Chem. Sci.*, 2019, **10**, 2413–2423.

30 C. R. Moylan, R. J. Twieg, V. Y. Lee, S. A. Swanson, K. M. Betterton and R. D. Miller, Nonlinear optical chromophores with large hyperpolarizabilities and enhanced thermal stabilities, *J. Am. Chem. Soc.*, 1993, **115**, 12599–12600.

31 C. W. Ghanavatkar, V. R. Mishra and N. Sekar, Review of NLOphoric azo dyes – Developments in hyperpolarizabilities in last two decades, *Dyes Pigm.*, 2021, **191**, 109367.

32 G. A. Timco, T. B. Faust, F. Tuna and R. E. P. Winpenny, Linking heterometallic rings for quantum information processing and amusement, *Chem. Soc. Rev.*, 2011, **40**, 3067–3075.

33 P. King, T. C. Stamatatos, K. A. Abboud and G. Christou, Reversible Size Modification of Iron and Gallium Molecular Wheels: A Ga_{10} "Gallic Wheel" and Large Ga_{18} and Fe_{18} Wheels, *Angew. Chem., Int. Ed.*, 2006, **45**, 7379–7383.

34 T. C. Stamatatos, A. G. Christou, C. M. Jones, B. J. O'Callaghan, K. A. Abboud, T. A. O'Brien and G. Christou, "Squaring the Circle": Molecular Squares and Rectangles from Chelate-Induced Structural Transformations of Known Fe_{10} and New Fe_{12} Ferric Wheels, *J. Am. Chem. Soc.*, 2007, **129**, 9840–9841.

35 D. Schray, G. Abbas, Y. Lan, V. Mereacre, A. Sundt, J. Dreiser, O. Waldmann, G. E. Kostakis, C. E. Anson and A. K. Powell, Combined Magnetic Susceptibility Measurements and ^{57}Fe Mössbauer Spectroscopy on a Ferromagnetic $\{FeIII_4Dy_4\}$ Ring, *Angew. Chem., Int. Ed.*, 2010, **49**, 5185–5188.

36 L. Qin, J. Singleton, W.-P. Chen, H. Nojiri, L. Engelhardt, R. E. P. Winpenny and Y.-Z. Zheng, Quantum Monte Carlo Simulations and High-Field Magnetization Studies of Antiferromagnetic Interactions in a Giant Hetero-Spin Ring, *Angew. Chem., Int. Ed.*, 2017, **56**, 16571–16574.

37 G. A. Timco, A. Fernandez, A. K. Kostopoulos, C. A. Muryn, R. G. Pritchard, I. Strashnov, I. J. Vitorica-Yrezebal, G. F. S. Whitehead and R. E. P. Winpenny, An Extensive Family of Heterometallic Titanium(IV)–Metal(III) Rings with Structure Control through Templates, *Angew. Chem., Int. Ed.*, 2017, **56**, 13629–13632.

38 W.-P. Chen, P.-Q. Liao, P.-B. Jin, L. Zhang, B.-K. Ling, S.-C. Wang, Y.-T. Chan, X.-M. Chen and Y.-Z. Zheng, The Gigantic {$Ni_{36}Gd_{102}$} Hexagon: A Sulfate-Templated "Star-of-David" for Photocatalytic CO_2 Reduction and Magnetic Cooling, *J. Am. Chem. Soc.*, 2020, **142**, 4663–4670.

39 H.-L. Zhang, Y.-Q. Zhai, H. Nojiri, C. Schröder, H.-K. Hsu, Y.-T. Chan, Z. Fu and Y.-Z. Zheng, {Sc_nGd_n} Heterometallic Rings: Tunable Ring Topology for Spin-Wave Excitations, *J. Am. Chem. Soc.*, 2022, **144**, 15193–15202.

40 J. Ferrando-Soria, A. Fernandez, E. Moreno Pineda, S. A. Varey, R. W. Adams, I. J. Vitorica-Yrezabal, F. Tuna, G. A. Timco, C. A. Muryn and R. E. P. Winpenny, Controlled Synthesis of Nanoscopic Metal Cages, *J. Am. Chem. Soc.*, 2015, **137**, 7644–7647.

41 J. Ferrando-Soria, A. Fernandez, D. Asthana, S. Nawaz, I. J. Vitorica-Yrezabal, G. F. S. Whitehead, C. A. Muryn, F. Tuna, G. A. Timco, N. D. Burton and R. E. P. Winpenny, A [13]rotaxane assembled via a palladium molecular capsule, *Nat. Commun.*, 2019, **10**, 3720.

42 M.-H. Du, S.-H. Xu, G.-J. Li, H. Xu, Y. Lin, W.-D. Liu, L.-S. Long, L.-S. Zheng and X.-J. Kong, Hierarchical Assembly of Coordination Macromolecules with Atypical Geometries: $Gd_{44}Co_{28}$ Crown and $Gd_{95}Co_{60}$ Cage, *Angew. Chem., Int. Ed.*, 2022, **61**, e202200537.

43 C. J. Pedersen, Cyclic polyethers and their complexes with metal salts, *J. Am. Chem. Soc.*, 1967, **89**, 2495–2496.

44 C. J. Pedersen, The Discovery of Crown Ethers, *Science*, 1988, **241**, 536–540.

45 A. Ikeda and S. Shinkai, Novel Cavity Design Using Calix[n] arene Skeletons: Toward Molecular Recognition and Metal Binding, *Chem. Rev.*, 1997, **97**, 1713–1734.

46 T. Hishiya, H. Asanuma and M. Komiyama, Spectroscopic Anatomy of Molecular-Imprinting of Cyclodextrin. Evidence for Preferential Formation of Ordered Cyclodextrin Assemblies, *J. Am. Chem. Soc.*, 2002, **124**, 570–575.

47 K. I. Assaf and W. M. Nau, Cucurbiturils: from synthesis to high-affinity binding and catalysis, *Chem. Soc. Rev.*, 2015, **44**, 394–418.

48 T. Ogoshi, T.-a. Yamagishi and Y. Nakamoto, Pillar-Shaped Macrocyclic Hosts Pillar[n]arenes: New Key Players for Supramolecular Chemistry, *Chem. Rev.*, 2016, **116**, 7937–8002.

49 M. V. Rekharsky and Y. Inoue, Complexation Thermodynamics of Cyclodextrins, *Chem. Rev.*, 1998, **98**, 1875–1918.

50 G. W. Gokel, W. M. Leevy and M. E. Weber, Crown Ethers: Sensors for Ions and Molecular Scaffolds for Materials and Biological Models, *Chem. Rev.*, 2004, **104**, 2723–2750.

51 K. Jie, Y. Zhou, E. Li, Z. Li, R. Zhao and F. Huang, Reversible Iodine Capture by Nonporous Pillar[6]arene Crystals, *J. Am. Chem. Soc.*, 2017, **139**, 15320–15323.

52 S. Yoon, J. Calvo and M. So, Removal of Acid Orange 7 from Aqueous Solution by Metal-Organic Frameworks, *Crystals*, 2018, **9**, 17.

53 P. J. Stephens, F. J. Devlin, C. F. Chabalowski and M. J. Frisch, Ab Initio Calculation of Vibrational Absorption and Circular Dichroism Spectra Using Density Functional Force Fields, *J. Phys. Chem.*, 1994, **98**, 11623–11627.

54 M. Zhou, Z. Ju and D. Yuan, A new metal–organic framework constructed from cationic nodes and cationic linkers for highly efficient anion exchange, *Chem. Commun.*, 2018, **54**, 2998–3001.

55 C. B. Pinto, L. H. R. Dos Santos and B. L. Rodrigues, Response of Hirshfeld Surface to Structural Modifications in Transition-Metal Coordination Compounds, *Cryst. Growth Des.*, 2020, **20**, 4827–4838.

56 B. Shi, X. Pang, S. Li, H. Wu, J. Shen, X. Wang, C. Fan, L. Cao, T. Zhu, M. Qiu, Z. Yin, Y. Kong, Y. Liu, M. Zhang, Y. Liu, F. Pan and Z. Jiang, Short hydrogen-bond network confined on COF surfaces enables ultrahigh proton conductivity, *Nat. Commun.*, 2022, **13**, 6666.

57 X. Li, H. Zhang, J. Hou, R. Ou, Y. Zhu, C. Zhao, T. Qian, C. D. Easton, C. Selomulya, M. R. Hill and H. Wang, Sulfonated Sub-1 nm Metal–Organic Framework Channels with Ultrahigh Proton Selectivity, *J. Am. Chem. Soc.*, 2020, **142**, 9827–9833.

58 X. Meng, H.-N. Wang, S.-Y. Song and H.-J. Zhang, Proton-conducting crystalline porous materials, *Chem. Soc. Rev.*, 2017, **46**, 464–480.

59 H. Pan, H. Chu, X. Wang, Y. Li, S. Zhao, G. Li and D. Li, Optical nonlinearity of zeolitic imidazolate framework-67 in the near-infrared region, *Mater. Chem. Front.*, 2020, **4**, 2081–2088.

60 G.-H. Chen, Y.-P. He, Z.-R. Wang, Q.-H. Li, Z.-Z. Ma and J. Zhang, Tunable third-order nonlinear optical effect via modifying $Ti_4(embonate)_6$ cage-based ionic pairs, *Inorg. Chem. Front.*, 2022, **9**, 1984–1991.

61 M. Sheik-Bahae, A. A. Said, T. H. Wei, D. J. Hagan and E. W. V. Stryland, Sensitive measurement of optical nonlinearities using a single beam, *IEEE J. Quantum Electron.*, 1990, **26**, 760–769.

62 C. W. Ghanavatkar, V. R. Mishra and N. Sekar, Review of NLOphoric azo dyes – Developments in hyperpolarizabilities in last two decades, *Dyes Pigm.*, 2021, **191**, 109367.

63 D.-J. Li, Z.-G. Gu and J. Zhang, Auto-controlled fabrication of a metal-porphyrin framework thin film with tunable optical limiting effects, *Chem. Sci.*, 2020, **11**, 1935–1942.

64 C. Zheng, Y. Du, M. Feng and H. Zhan, Shape dependence of nonlinear optical behaviors of nanostructured silver and their silica gel glass composites, *Appl. Phys. Lett.*, 2008, **93**, 143108.

65 C. Zheng, X. Ye, S. Cai, M. Wang and X. Xiao, Observation of nonlinear saturable and reverse-saturable absorption in silver nanowires and their silica gel glass composite, *Appl. Phys. B*, 2010, **101**, 835–840.

66 D.-J. Li, Q.-h. Li, Z.-R. Wang, Z.-Z. Ma, Z.-G. Gu and J. Zhang, Interpenetrated Metal-Porphyrinic Framework for Enhanced Nonlinear Optical Limiting, *J. Am. Chem. Soc.*, 2021, **143**, 17162–17169.